

Article

The Promotional Effect of Na on Ru for pH-Universal Hydrogen Evolution Reactions

Bingxin Guo ¹, Chengfei Zhao ¹, Yingshuang Zhou ¹, Junjie Guo ^{2,*}, Zhongzhe Wei ^{3,*} and Jing Wang ^{1,*}

¹ College of Materials and Environmental Engineering, Institute of Advanced Magnetic Materials, Hangzhou Dianzi University, Hangzhou 310018, China

² Key Laboratory of Interface Science and Engineering in Advanced Materials, Ministry of Education, Taiyuan University of Technology, Taiyuan 030024, China

³ Institute of Industrial Catalysis, College of Chemical Engineering, Zhejiang University of Technology, Hangzhou 310032, China

* Correspondence: jguo@hdu.edu.cn (J.G.); weizhzh@zjut.edu.cn (Z.W.); chemwj@hdu.edu.cn (J.W.)

Abstract: Alkali metals, as ideal electron donors, can effectively regulate the valence state distribution of the host metals. Nevertheless, no studies have reported the application of alkali metal promoters in the hydrogen evolution reaction (HER). Here, we designed an efficient and wide pH-universal hydrogen evolution catalyst that utilizes alkali metal to control the valence, size, and dispersion of Ru NPs. The experimental results reveal that the alkali metal additives contribute to the dispersion and stabilization of metallic Ru. More importantly, the interaction between Na and Ru regulates the distribution of Ru valence states and helps to form more active components of Ru⁰. Additionally, NaCl functioned as an in situ template to assist the construction of a porous carbon skeleton promotes mass transfer and exposes more active sites, further promoting the synergistic effect of Ru and Na. As a result, the optimal Ru_{0.3}/C–800 delivers high efficiency for HER with an overpotential as low as 29 mV in 1.0 M KOH and 83 mV in 0.5 M H₂SO₄ under 10 mA cm^{−2}. Particularly, the catalytic performance of Ru_{0.3}/C–800 even outbalanced that of commercial Pt/C in an alkaline medium. This rational construction strategy opens up new avenues for obtaining superior pH-universal electrocatalysts.

Keywords: alkali metal; Ru based; hydrogen evolution reaction; wide-range pH; promotional effect



Citation: Guo, B.; Zhao, C.; Zhou, Y.; Guo, J.; Wei, Z.; Wang, J. The Promotional Effect of Na on Ru for pH-Universal Hydrogen Evolution Reactions. *Catalysts* **2023**, *13*, 552. <https://doi.org/10.3390/catal13030552>

Academic Editor: Bruno Fabre

Received: 15 February 2023

Revised: 4 March 2023

Accepted: 7 March 2023

Published: 9 March 2023



Copyright: © 2023 by the authors. Licensee MDPI, Basel, Switzerland. This article is an open access article distributed under the terms and conditions of the Creative Commons Attribution (CC BY) license (<https://creativecommons.org/licenses/by/4.0/>).

1. Introduction

As a sustainable secondary energy, hydrogen (H₂) energy has the advantages of wide raw material sources and zero carbon emission, and it has demonstrated an excellent application foreground in industries such as automotive, chemical, and aviation [1,2]. Compared with traditional steam reforming technology, producing hydrogen by water electrolysis fundamentally eliminates the dependence on fossil fuels and achieves zero carbon emissions [3,4]. Nowadays, the electrolysis of water has become the most competitive hydrogen production technology [5,6]. Alkaline electrolyzer, proton exchange membrane electrolyzer, and other types of electrolyzers are available on the market. The various operating environments put forward higher requirements for the design of catalysts. It is highly desirable to create economical and pH-universal catalysts. Moreover, the practical deployment of water electrolysis technology is heavily restricted by the sluggish kinetics of the cathode catalysts, which results in a high overpotential to drive H₂ production [7]. Currently, Pt-based electrocatalysts, as the benchmark for HER, exhibit excellent catalytic performance [8–11]. Unfortunately, the scarce reserves and exorbitant price largely impede their commercialization. Developing cost-effective electrocatalysts to substitute Pt/C is a central issue in the water industry [12]. As a Pt-group metal, Ru possesses a moderate metal–hydrogen bond strength similar to Pt–H, but the cost is only 1/30 that of

Pt [13–16]. In general, the HER efficiency is determined by the strength of the metal–hydrogen bond [17]. Ru serving as a catalyst’s active center instead of expensive Pt metal is expected to keep the catalytic activity unchanged while reducing the catalyst cost [18,19]. However, the current Ru-based catalysts suffer from complex preparation methods, the high toxicity of reagents, and high metal loading [20]. Therefore, it is urgent and challenging to develop facile, economical, and green synthetic strategies for fabricating efficient Ru-based catalysts.

Alkali metal, serving as a structural or electronic regulator, plays vital role in thermocatalytic reactions [21]. Since the first report on the promotional effect of alkali metal in 1845, the function of alkali metal has been systematically studied in hydrogenation reactions, such as ammonia production [22], Fischer–Tropsch process [23], aromatics [24], hydrogenation of unsaturated hydrocarbons [25–28], and CO₂ [29]. In the meantime, it is generally believed that alkali metals act as electron donors to modulate the electronic structures of the active metals, thereby changing the adsorption of reacting intermediates [30–32]. For example, Zhang introduced Na dopant and oxygen vacancy, which made the d-band center of RuO₂ far away from the Fermi level, resulting in the weakening of the chemical bond between the oxygen intermediate and the surface of RuO₂, thus reducing the activation barrier of the oxygen evolution reaction (OER) to optimize the performance [33]. By regulating the interplay of Na and Co, Wu’s group obtained stable Na–Co₂C active sites, formed Na–CO bonds to strengthen the interaction between Na and Co₂C, dispersed the Co₂C, and reduced the particle size [34]. Despite alkali metal promoters being widely used in thermocatalysis, OER, etc., the application of alkali metal promoters in HER has not been reported, let alone the influencing mechanism of alkali metal on the HER performance.

Herein, “starch strips” derived from potatoes, commercially used in the preparation of puffed food were chosen as the carbon source. The “starch strips” were economical, widely sourced, and rich in NaCl. Utilizing abundant NaCl in “starch strips” as the pore-forming agent, the porous carbon-supported ultra-dispersed Ru-based composite (Ru/C) was synthesized by a simple impregnation–pyrolysis strategy; meanwhile, alkali metal Na promoters were introduced in situ. It was found that the introduction of Na greatly modulated the valence state distribution of Ru species, inducing the formation of more Ru⁰ states which, in turn, boosted the electrocatalytic performance. Benefitting from the interplay between Na and Ru, as well as the developed texture structure, Ru_{0.3}/C–800 functioned as a super and long-lasting HER catalyst over a broad pH range. In 1.0 M KOH and 0.5 M H₂SO₄, the overpotentials of Ru_{0.3}/C–800 were only 29 mV and 83 mV to achieve the current density of 10 mA cm^{−2}. Notably, the mass loading of Ru in Ru_{0.3}/C–800 was as low as 0.81 wt%, greatly reducing the synthetic cost compared with that of commercial Pt/C (20 wt%). Furthermore, the HER performance for Ru_{0.3}/C–800 outbalanced Pt/C in alkaline solution. This work provides a new method for alkali metal promoters to tune the electrocatalytic performance, which could lead to the design of novel catalysts for efficient hydrogen evolution.

2. Results and Discussion

2.1. Catalyst Synthesis and Characterization

The Ru/C was synthesized using the method of impregnation adsorption and one-step pyrolysis starting from RuCl₃ and “starch strips” derived from potatoes as the feedstock, which was ecofriendly, commercially available, and inexpensive (Figure 1). Benefitting from the confinement effect of the carbon skeleton, Ru species were converted into monodispersed nanoparticles (NPs) [35]. In this study, the as-prepared catalysts were named Ru_x/C–T, where x refers to the additional amounts of Ru (0, 0.2, 0.3, and 0.4 mmol), and T refers to pyrolysis temperature (700, 800, 900, and 1000 °C). Transmission electron microscopy (TEM) was performed to observe their morphologies and microstructures. For Ru_{0.3}/C–800, a distinct pore structure was exhibited on the carbon substrate (Figure S1), which was attributed to the pore-forming effect of NaCl. It was not difficult to find that, the Ru NPs of Ru_{0.3}/C–800 were uniformly distributed on the carbon frame with a mean

particle size of ~ 1.90 nm (Figure 2a). When the dose of Ru^{3+} was lower than 0.4 mmol, the Ru particles of $\text{Ru}_{0.2}/\text{C}-800$ had a uniform size. However, upon increasing the addition of Ru^{3+} to 0.4 mmol, the Ru particles of $\text{Ru}_{0.4}/\text{C}-800$ were significantly agglomerated (Figure S2). In addition, the pyrolysis temperature also played a vital part in the distribution of Ru particles. As displayed in Figure S3a, $\text{Ru}_{0.3}/\text{C}-700$ displayed the homogeneous distribution of Ru NPs due to the fact of insufficient nucleation under low pyrolysis temperature. However, with the increase in the pyrolysis temperature, the agglomeration of the Ru NPs occurred obviously (Figure S3b,c). Furthermore, to investigate the role of NaCl on the microstructure and metal phase of the catalysts, the “starch sticks” were pretreated to wash off NaCl as much as possible, and the obtained catalyst was denoted as $\text{Ru}_{0.3}/\text{C}-800\text{-WF}$. Compared with $\text{Ru}_{0.3}/\text{C}-800$, the pore structure of $\text{Ru}_{0.3}/\text{C}-800\text{-WF}$ was not obvious at the same scale, indicating the pore-forming effect of NaCl. In addition, $\text{Ru}_{0.3}/\text{C}-800\text{-WF}$ only contained a small number of Ru particles, which demonstrates that NaCl also contributed to dispersing and anchoring the metallic Ru (Figure S4). The mass loading of Ru and Na was, furthermore, measured by an inductively coupled plasma-optical emission spectrometer (ICP-OES). As elevating the pyrolysis temperature from 800 °C to 1000 °C, the Na content gradually reduced from 0.36 wt% to 0.004 wt% (Table S1). Accordingly, the content of Ru showed the same variation trend as that of Na content with the decreased content from 0.81 wt% to 0.11 wt%. Similarly, the Ru content of $\text{Ru}_{0.3}/\text{C}-800\text{-WF}$ was reduced as the Na content decreased compared with $\text{Ru}_{0.3}/\text{C}-800$. Such results revealed that the stabilizing effect of Na on Ru was due to the interaction between them. Detected by high-resolution transmission electron microscopy (HRTEM), the interplanar spacings of $\text{Ru}_{0.3}/\text{C}-800$ were measured to be 0.205 nm and 0.231 nm (Figure 2b), coincident with the (101) and (100) planes of Ru, respectively. In addition, the uniform distribution of metallic Ru in the carbon matrix was further identified under a high-angle annular dark-field scanning transmission electron microscope (HAADF-STEM) (Figure 2c) [36]. The elemental mapping of $\text{Ru}_{0.3}/\text{C}-800$ (Figure 2d – i) demonstrated the homogeneous dispersion of C, O, N, Ru, Na, and Cl. Notably, it could be found that the element Ru was distributed around Na, as shown in the Figure S5, indicating the interaction between them, to a certain extent.

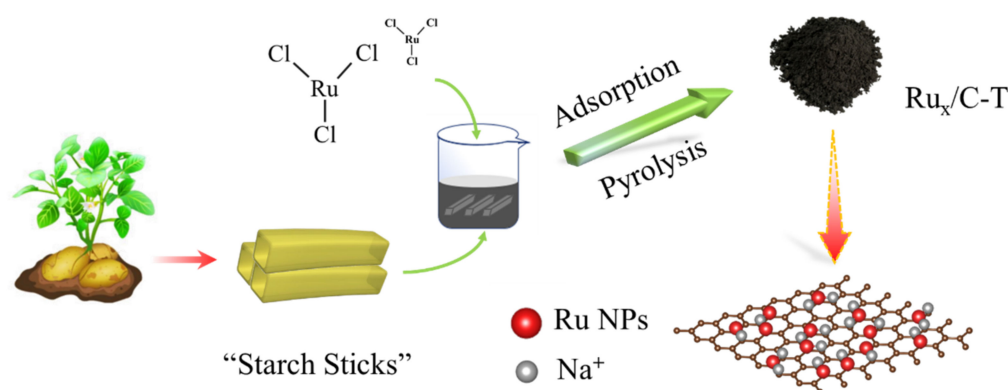


Figure 1. The synthetic procedure for $\text{Ru}_x/\text{C}-\text{T}$ catalysts.

More structural details of the catalysts were then confirmed by X-ray diffractometer (XRD). From Figure 3a, a broad peak belonging to amorphous carbon was observed in all samples. Apart from that, the diffraction peaks coincided well with the (100), (002), and (101) planes of Ru (PDF#06-0663) located at $\approx 38.4^\circ$, 42.2° , and 44.0° , which appeared in $\text{Ru}_{0.3}/\text{C}-800$ and $\text{Ru}_{0.3}/\text{C}-900$. This result was associated with the good crystalline character of Ru at 800 °C and 900 °C (Figure S6). In addition, the typical diffraction peaks of NaCl (PDF#05-0628) at $\approx 31.7^\circ$ and 45.5° were presented as well. It was worth noting that the intensity of the NaCl peaks weakened obviously along with the elevated pyrolysis temperature, which was due to the volatilization of NaCl as the temperature increased [37]. As for $\text{Ru}_{0.3}/\text{C}-800\text{-WF}$, there were only amorphous carbon peaks existing from the

XRD pattern, revealing that NaCl was completely removed (Figure S7b). Moreover, as exhibited in Figure S7a, the NaCl peak intensity gradually weakened as the content of in Ru content increased.

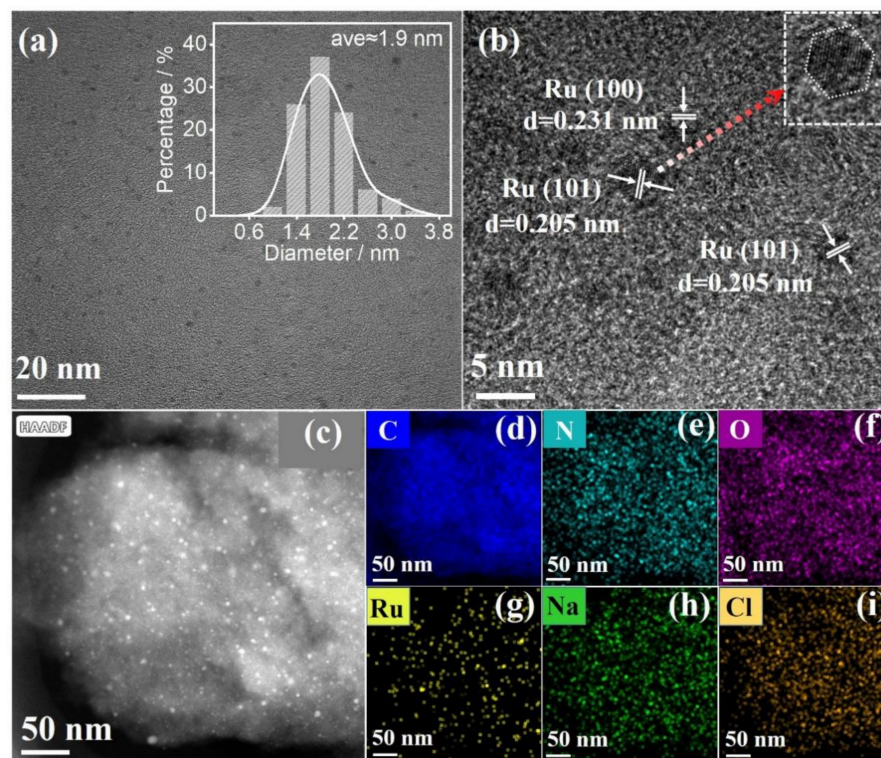


Figure 2. (a) TEM image of Ru_{0.3}/C–800 (inset: the corresponding Ru NPs size distribution histogram); (b) HRTEM image of Ru_{0.3}/C–800; (c) HAADF-STEM image of Ru_{0.3}/C–800; (d–i) Elemental mappings for C, N, O, Ru, Na, and Cl in Ru_{0.3}/C–800, respectively.

X-ray photoelectron spectroscopy (XPS) was further employed to reveal the chemical valence and elemental compositions of the samples [17]. Here, the C 1s peak of 284.5 eV served as the standard for all of the peaks' calibration [38]. Figure 3b visually showed the Na 1s peaks of Ru_{0.3}/C–800 and C–800. In contrast to C–800, the Na 1s peak of Ru_{0.3}/C–800 was shifted towards higher binding energy owing to the electron transfer from Na to Ru. From the Ru 3p spectra in Figure 3c, the peaks at 462.0 eV, 484.2 eV, 464.6 eV, and 486.5 eV were corresponding to Ru⁰ 3p_{3/2}, Ru⁰ 3p_{1/2}, Ruⁿ⁺ 3p_{3/2}, and Ruⁿ⁺ 3p_{1/2}, respectively [17,39]. The binding energy of Ru 3p of Ru_{0.3}/C–800 was negatively biased compared with Ru_{0.3}/C–800–WF. Moreover, the peak positions of Na 1s and Ru 3p varied with the pyrolysis temperature. As shown in Figure S8a, with the increase in the temperature, Na 1s shifted to the low binding energy. In Figure S8b, when the content of Na is high, the shift in the Ru 3p peak position was more obvious, because more Na transferred electrons to Ru. It was calculated that the ratio of Ru⁰/Ruⁿ⁺ for Ru_{0.3}/C–800 was 1.68, which was much higher than that of other control groups (Table S2). According to reports, Ru⁰ was the active center of catalytic hydrogen production, and the high content of Ru⁰ was helpful for improving catalytic hydrogen production [40]. In this system, Na, as an electronic structure regulator, could effectively adjust the valence distribution of Ru, promoting the formation of more Ru⁰, and hopefully improved catalytic activity.

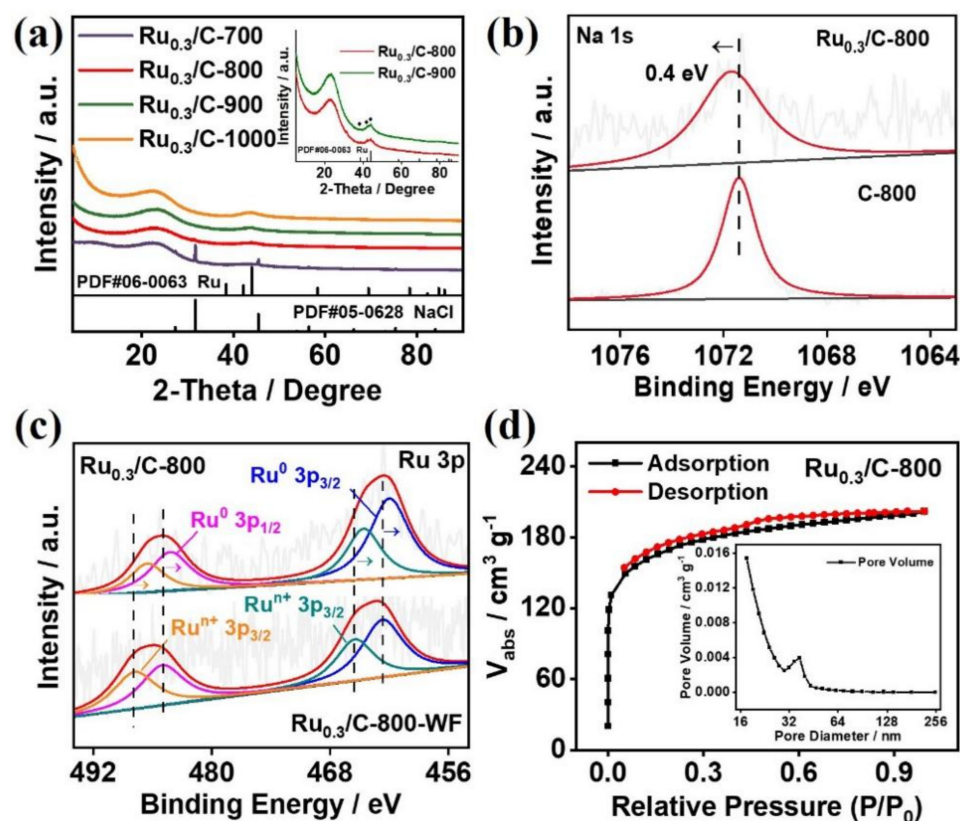


Figure 3. (a) XRD patterns of $\text{Ru}_{0.3}/\text{C}-700$, $\text{Ru}_{0.3}/\text{C}-800$, $\text{Ru}_{0.3}/\text{C}-900$, and $\text{Ru}_{0.3}/\text{C}-1000$; (b) XPS spectra of Na 1s of $\text{Ru}_{0.3}/\text{C}-800$ and C-800; (c) XPS spectra of Ru 3p of $\text{Ru}_{0.3}/\text{C}-800$ and $\text{Ru}_{0.3}/\text{C}-800\text{-WF}$; (d) N_2 adsorption/desorption curves of $\text{Ru}_{0.3}/\text{C}-800$ (inset: pore size distribution plot).

Na not only served as an assistant to regulate the valence distribution of Ru and increase the content of Ru^0 but also acted as a pore-forming agent that could affect the pore structure of the catalysts [41]. The pore structure was studied using the Brunauer–Emmett–Teller (BET) method, as displayed in Figure 3d. The N_2 adsorption/desorption plots exhibited that the specific surface area of $\text{Ru}_{0.3}/\text{C}-800$ was $592.0 \text{ m}^2 \text{ g}^{-1}$, significantly larger than other catalysts (Table S3). The decreased specific surface areas of $\text{Ru}_{0.3}/\text{C}-900$ and $\text{Ru}_{0.3}/\text{C}-1000$ were possibly caused by the collapse of the mesoporous structure when the material calcined at high temperatures (especially over $800 \text{ }^\circ\text{C}$). Furthermore, the pore size distribution of $\text{Ru}_{0.3}/\text{C}-800$ (inset in Figure 3d) manifested a large number of mesopores. The existence of a large number of mesopores was beneficial for the solution to enter during the reaction, which increased the contact area, exposed more active sites, and accelerated mass transfer [42]. Additionally, the defective nature of the catalysts was investigated by Raman spectroscopy [43]. A typical D band and G band of carbon was manifested in $\text{Ru}_{0.3}/\text{C}-800$, and the intensity ratio I_D/I_G was 0.856. Moreover, the value of I_D/I_G increased with the increase in the pyrolysis temperatures (Figure S9), possibly because too high pyrolysis temperature would lead to the collapse of the pore structure. It displayed that only an appropriate pyrolysis temperature can optimize the conductivity, as well as the catalytic abilities of the composites.

2.2. Electrochemical Characterization

The Ru powder, commercial Pt/C (20 wt%), Pt electrode, and $\text{Ru}_x/\text{C}-\text{T}$ were tested for HER in 1.0 M KOH, 0.5 M H_2SO_4 , and 1.0 M PBS, respectively. As is well known, the HER activity was evaluated by the overpotential (η_{10}) at the current density of 10 mA cm^{-2} [43–46]. From Figure 4a, the blank carbon (C-800) displayed almost no activity for hydrogen generation within the applied potential window. However, upon

introducing trace Ru in the system, the catalytic activity was significantly improved. With the increase in the Ru concentration, the η_{10} distinctly declined from 73 mV ($\text{Ru}_{0.2}/\text{C}-800$) to 29 mV ($\text{Ru}_{0.3}/\text{C}-800$). Whereas, the η_{10} further increased to 35 mV ($\text{Ru}_{0.4}/\text{C}-800$) when the Ru dosage was increased to 0.4 mmol. These results indicate that the appropriate Ru content was able to enhance the catalytic activity. It is noteworthy that the HER of $\text{Ru}_{0.3}/\text{C}-800$ exhibited an even better performance than Pt/C (20 wt%), Ru powder, and Pt electrode in 1.0 M KOH, as shown in Figures 4a and S10. Additionally, an effective catalyst for HER was able to initiate proton reduction with minimum overpotential and fast kinetics [46]. Normally, the Tafel slope is a vital indicator to investigate the reaction kinetics for HER [47]. According to the polarization curves of the samples, the corresponding Tafel slopes were obtained (Figure 4b). It was not hard to find that the order of Tafel slopes was $\text{Ru}_{0.3}/\text{C}-800$ ($34.43 \text{ mV dec}^{-1}$) < $\text{Ru}_{0.4}/\text{C}-800$ ($36.89 \text{ mV dec}^{-1}$) < Pt/C ($59.44 \text{ mV dec}^{-1}$) < $\text{Ru}_{0.2}/\text{C}-800$ ($78.74 \text{ mV dec}^{-1}$), which was in line with the trend of η_{10} . The smaller Tafel slope value of $\text{Ru}_{0.3}/\text{C}-800$ suggested a higher reaction rate, and the HER catalyzed by $\text{Ru}_{0.3}/\text{C}-800$ followed a Volmer–Heyrovsky mechanism [12]. Then, the charge transfer kinetics involved in HER was detected through EIS. The subsequent Nyquist diagram (Figure 4c) demonstrated that the curve of the sample was virtually semicircular, with the diameter of the curve standing for the associated charge transfer resistance (R_{ct}). In addition, the lower R_{ct} indicated a rapid electrode reaction rate. The $\text{Ru}_{0.3}/\text{C}-800$ had the smallest R_{ct} , indicating that the reaction rate was the fastest, which was consistent with the results of the voltammetry measurements. Furthermore, the electrochemical double-layer capacitance (C_{dl}), which was measured in the non-Faraday region of the CV curves, was used to evaluate the ECSA. The C_{dl} value was produced by linearly graphing the capacitance current density response vs. the scanning rate [17]. Figure S11 depicts the ECSA curves with various Ru contents. The C_{dl} of $\text{Ru}_{0.3}/\text{C}-800$ was $135.66 \text{ mF cm}^{-2}$ (Figure 4d), which was significantly higher than the C_{dl} of $\text{Ru}_{0.4}/\text{C}-800$ ($113.54 \text{ mF cm}^{-2}$), $\text{Ru}_{0.2}/\text{C}-800$ (65.31 mF cm^{-2}), and C-800 (4.60 mF cm^{-2}). The increase in the C_{dl} value means that $\text{Ru}_{0.3}/\text{C}-800$ possesses a large active surface area, which contributes to the exposure of active sites and the charge transfer [48].

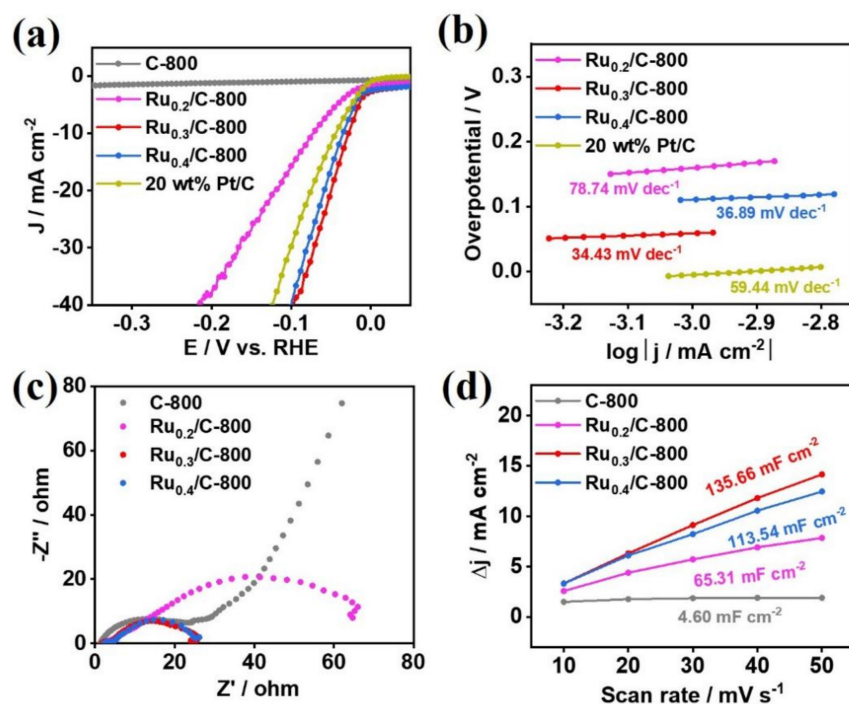


Figure 4. (a) LSV curves of C-800, $\text{Ru}_{0.2}/\text{C}-800$, $\text{Ru}_{0.3}/\text{C}-800$, $\text{Ru}_{0.4}/\text{C}-800$, and 20 wt% Pt/C in 1.0 M KOH; (b) Tafel plots of C-800, $\text{Ru}_{0.2}/\text{C}-800$, $\text{Ru}_{0.3}/\text{C}-800$, $\text{Ru}_{0.4}/\text{C}-800$, and 20 wt% Pt/C in 1.0 M KOH; (c) Nyquist plots of C-800, $\text{Ru}_{0.2}/\text{C}-800$, $\text{Ru}_{0.3}/\text{C}-800$ and $\text{Ru}_{0.4}/\text{C}-800$ in 1.0 M KOH; (d) linear plot of the capacitive current against the scan rate for the estimation of C_{dl} .

On this basis, the role of the pyrolysis temperature on the catalytic activity was subsequently explored [18]. As shown in Figure 5a, Ru_{0.3}/C-700 presented a high overpotential of 214 mV in alkaline solution to achieve 10 mA cm⁻². Upon increasing the pyrolysis temperature, the overpotential dropped sharply, and the overpotential of Ru_{0.3}/C-800 only required 29 mV to achieve the same current density. However, further elevating the pyrolysis temperature, the overpotential increased to 52 mV and 90 mV for Ru_{0.3}/C-900 and Ru_{0.3}/C-1000, respectively. Additionally, as exhibited in Figure S12, the C_{dl} value rose first and then declined with the increase of the pyrolysis temperature. This result was in line with the activity trend. It was further confirmed that the high C_{dl} was the reason for the improved activity. However, the variation in the C_{dl} mainly came from the specific surface area, which was ultimately ascribed to the NaCl template for the forming of pores. Furthermore, the catalytic activity was closely correlated with the electrochemical reaction rate and the capability of charge transfer, which was verified by the Tafel (Figure 5b) and EIS (Figure 5c) results. In addition, Figure S13 illustrates the EIS fitting circuit for Ru_{0.3}/C-800, Ru_{0.3}/C-900, and Ru_{0.3}/C-1000 in 1.0 M KOH. It can be seen from Table S4 that the smaller R_{ct} value of Ru_{0.3}/C-800 corresponded to the higher reaction rates. More importantly, the overpotential of Ru_{0.3}/C-800-WF increased to 72 mV when the amount of NaCl in the raw material was washed off (Figure 5d), and Figure S14 shows that the corresponding Tafel, C_{dl}, and EIS results displayed a worsening trend. This was due to the pore-forming effect of NaCl, which regulated the specific surface area of the catalysts and, thus, affected their activity. Meanwhile, it can be seen from Figure 5e that the decrease in the NaCl content in the raw materials was accompanied by the decrease in the Ru⁰ component and the deterioration of activity. Moreover, the same results can be obtained from the catalysts calcined under varied temperatures. When the pyrolysis temperature rose, the overpotential for Ru_{0.3}/C-800, Ru_{0.3}/C-900, and Ru_{0.3}/C-1000 at 10 mA cm⁻² was inversely proportional to the Ru⁰ content. To put it simply, the higher the Ru⁰ content, the smaller the overpotential of the catalyst, and the better the electrochemical performance. These findings again demonstrate the interaction between Na and Ru; that is, Na not only adjusted the valence state of the Ru phase but also stabilized Ru. Simultaneously, an ideal catalyst not only has excellent catalytic activity but also high catalytic stability. Therefore, stability was another vital indicator to assess the performance of the catalyst [49–51]. On the one hand, the durability of Ru_{0.3}/C-800 was measured by continuous CV sweeps. Figure 5f reveals that the overpotential only fell by 2 mV after 1000 cycles, suggesting the excellent stability of Ru_{0.3}/C-800. On the other hand, under the corresponding potential, a further measurement was performed for 10 h by chronoamperometry. No significant reduction in the current density could be observed (inset in Figure 5f).

Furthermore, we also studied the electrocatalytic activity of the catalyst in acidic and neutral media, verifying the universality of the designed catalyst in a wide pH [52]. In acidic medium, a current density of 10 mA cm⁻² could be reached by the low overpotential of 83 mV for Ru_{0.3}/C-800, which was significantly lower than that of Ru_{0.3}/C-700 (basically inactivated), Ru_{0.3}/C-900 (96 mV), and Ru_{0.3}/C-1000 (131 mV). Meanwhile, the corresponding Tafel slope and EIS plots (Figure 5h,i) showed the same trend as the activity curves. Additionally, the activity of Ru_{0.3}/C-800 was better than Ru powder in acidic medium (Figure S15a), and Ru_{0.3}/C-800 exhibited good stability (Figure S15b). Moreover, we conducted activity tests in a neutral environment (Figure S16a). The performance was not ideal, but Ru_{0.3}/C-800 still had advantages compared with the Ru powder. Surprisingly, the performance of Ru_{0.3}/C-800 was excellent in terms of stability (Figure S16b). In summary, the above results strongly support the hypothesis that Ru_{0.3}/C-800 has good activity and stability for HER in a wide pH range.

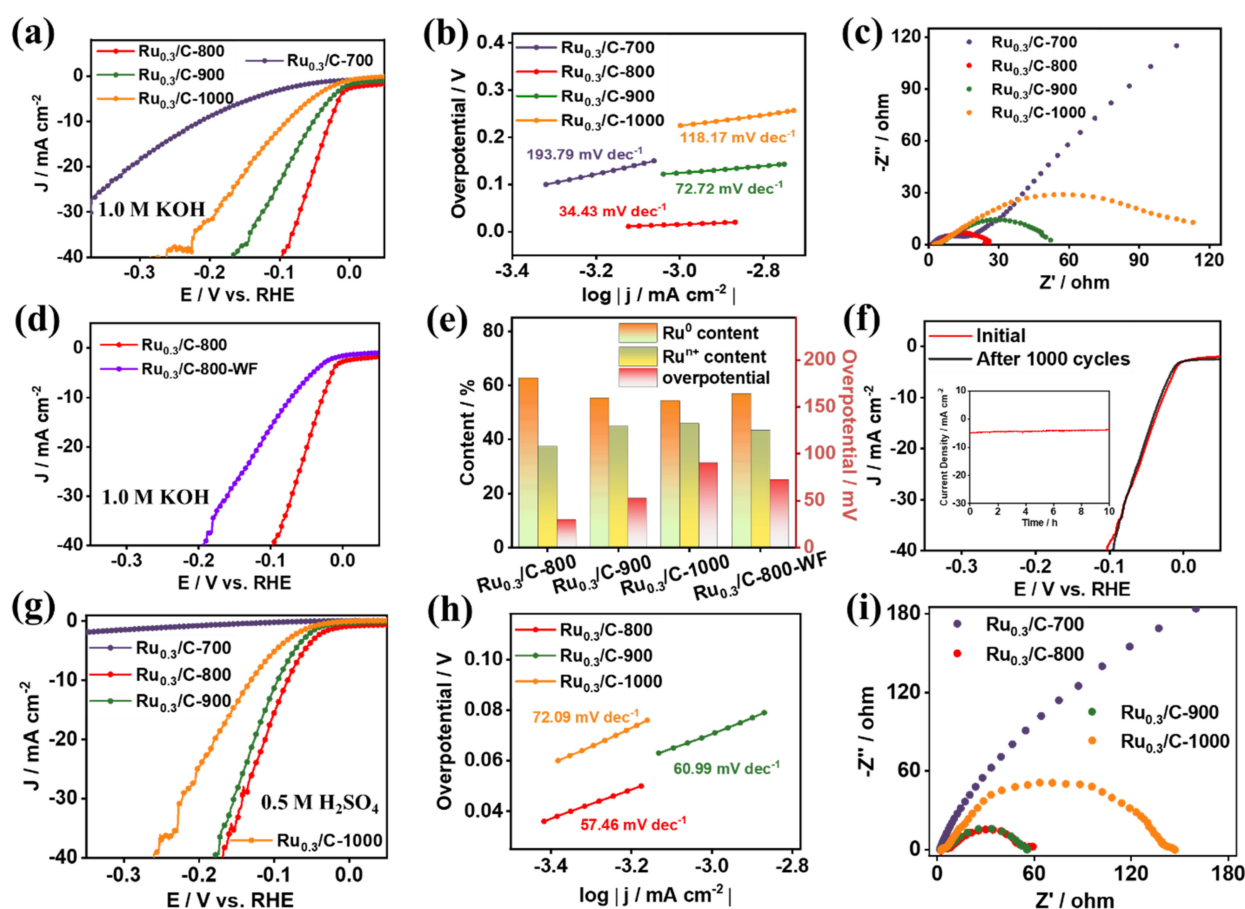


Figure 5. (a) LSV curves of $\text{Ru}_{0.3}/\text{C}-700$, $\text{Ru}_{0.3}/\text{C}-800$, $\text{Ru}_{0.3}/\text{C}-900$, and $\text{Ru}_{0.3}/\text{C}-1000$ in 1.0 M KOH; (b) Tafel plots of $\text{Ru}_{0.3}/\text{C}-700$, $\text{Ru}_{0.3}/\text{C}-800$, $\text{Ru}_{0.3}/\text{C}-900$, and $\text{Ru}_{0.3}/\text{C}-1000$; (c) Nyquist plots of $\text{Ru}_{0.3}/\text{C}-700$, $\text{Ru}_{0.3}/\text{C}-800$, $\text{Ru}_{0.3}/\text{C}-900$, and $\text{Ru}_{0.3}/\text{C}-1000$; (d) LSV curves of $\text{Ru}_{0.3}/\text{C}-800$ and $\text{Ru}_{0.3}/\text{C}-800\text{-WF}$ in 1.0 M KOH; (e) relationship diagram of Ru^0 content and Ru^{II} content and overpotential of $\text{Ru}_{0.3}/\text{C}-800$, $\text{Ru}_{0.3}/\text{C}-900$, $\text{Ru}_{0.3}/\text{C}-1000$, and $\text{Ru}_{0.3}/\text{C}-800\text{-WF}$; (f) LSV curves of $\text{Ru}_{0.3}/\text{C}-800$ before and after 1000 CV tests (inset: the i - t curve of $\text{Ru}_{0.3}/\text{C}-800$); (g) LSV curves of $\text{Ru}_{0.3}/\text{C}-700$, $\text{Ru}_{0.3}/\text{C}-800$, $\text{Ru}_{0.3}/\text{C}-900$, and $\text{Ru}_{0.3}/\text{C}-1000$ in 0.5 M H_2SO_4 ; (h) Tafel plots of $\text{Ru}_{0.3}/\text{C}-800$, $\text{Ru}_{0.3}/\text{C}-900$, and $\text{Ru}_{0.3}/\text{C}-1000$; (i) Nyquist plots of $\text{Ru}_{0.3}/\text{C}-700$, $\text{Ru}_{0.3}/\text{C}-800$, $\text{Ru}_{0.3}/\text{C}-900$, and $\text{Ru}_{0.3}/\text{C}-1000$.

3. Experimental

3.1. Chemicals

Potassium hydroxides (KOH), ruthenium (III) chloride (RuCl_3 , Ru content: 45 wt%~55 wt%), sulfuric acid (H_2SO_4), Ru powder, and ethanol were bought from Aladdin Industrial Inc. The commercial Pt/C with 20 wt% Pt loading was purchased from Johnson Matthey Company (Sigma, Shanghai, China). The main ingredient in the “starch strips” was starch, which was bought from supermarkets and is usually used in the production of puffed foods. Deionized water (DIW) was used to prepare all solutions. The DIW used in the experiment was obtained using a water purifier Hitech-DW, Wenzhou, Zhejiang Province, China).

3.2. Synthesis of Electrocatalysts

3.2.1. Synthesis of $\text{Ru}_{0.3}/\text{C}-800$

First, 400 mg of RuCl_3 was weighed and dissolved in 20 mL of DIW. Another clean glass beaker was used and 17 mL of DIW was mixed with 3 mL of the prepared RuCl_3 solution. After, ~4 g of the “starch strips” were soaked in the above RuCl_3 solution at room temperature for 1 h. Furthermore, the treated “starch strips” were transferred to

a watchglass and dried at 60 °C to obtain the precursor. Afterward, the precursor was calcined at 800 °C for 2 h in a tube furnace under an Ar environment. Finally, the product was ultrasonically washed several times with DIW. The final product, Ru_{0.3}/C–800, was obtained after drying.

3.2.2. Synthesis of C–800, Ru_{0.2}/C–800, and Ru_{0.4}/C–800

For the comparison of the samples of C–800, Ru_{0.2}/C–800, and Ru_{0.4}/C–800, the total volume of the reaction mixture remained at 20 mL. However, the addition of the RuCl₃ solution was changed to 0/2/4 mL, respectively. The other conditions remained unchanged.

3.2.3. Synthesis of Ru_{0.3}/C–700, Ru_{0.3}/C–900, and Ru_{0.3}/C–1000

For the comparison of the samples of Ru_{0.3}/C–700, Ru_{0.3}/C–900, and Ru_{0.3}/C–1000, the preparation procedure followed that of Ru_{0.3}/C–800, except that the calcination temperature varied to 700 °C, 900 °C, and 1000 °C.

3.2.4. Synthesis of Ru_{0.3}/C–800–WF (Wash First)

In addition, to demonstrate the influence of Na on the valence state of Ru, a control sample was set. In the early stage, the NaCl in the “starch strips” were washed as much as possible, and then the washed “starch strips” were used as raw materials for the synthesis of Ru_{0.3}/C–800–WF. The preparation process followed that of Ru_{0.3}/C–800.

3.3. Material Characterization

The HRTEM was carried out on a Talos F200S S-Twin (Thermo Fisher, Czech Republic), and the accelerating voltage was 200 kV. A D/tex Ultima TV wide-angle X-ray diffractometer (NIC, Japan) was employed to measure the metal phase of the samples. The diffractometer was equipped with Cu K α radiation (1.54 Å), and the scanning rate was 5 °/min. The Raman spectra were collected on a Raman spectrometer (Labram HR800-LS55, HORIBA, France). The specific surface area and PSD curves were calculated by traditional BET and BJH methods, respectively. The X-ray photoelectron spectra (XPS) for the bonding states were obtained using a Thermo ESCALAB 250xi spectrometer (Thermo Fisher, Czech Republic). In addition, the samples were first dissolved with aqua regia. Inductively coupled plasma-optical emission spectrometry (ICP-OES) (PerkinElmer, Optima 5300 DV) was used to measure the contents of Ru and Na. The Ru content of Ru_{0.3}/C-800 was as low as 0.81 wt% as measured by ICP-OES.

3.4. Electrochemical Characterization

To assess the HER performance of the catalysts, all experiments were performed on a conventional three-electrode system with CHI 760E as the electrochemical workstation, and the temperature during the test was kept at room temperature. A saturated calomel electrode (SCE) and a carbon rod was employed as the reference and the counter electrode, respectively. A glassy carbon electrode 5 mm in diameter acted as the working electrode. A 3 mg catalyst was dispersed in the mixture of Nafion (20 μ L) and ethanol (300 μ L). Whereafter, the prepared ink was ultrasonic treated for 30 min to form a uniform suspension. Then, 30 μ L ink was coated on the surface of the glassy carbon electrode and dried at room temperature. The electrochemical tests were operated in 0.5 M H₂SO₄, 1.0 M KOH, and 1.0 M PBS solution. Linear sweep voltammogram (LSV) curves were acquired at a scan rate of 5 mV s^{−1} over a potential window of −0.4 to 0.1 V (relative to a reversible hydrogen electrode (RHE)). All polarization curves were IR-corrected. The Tafel equation ($\eta = a + b \log(j)$) was employed to fit the slope of Tafel. In order to obtain the electrochemical active surface area (ECSA) of the prepared catalysts, we measured a series of cyclic voltammetry (CV) plots at different scanning rates from 10 to 50 mV s^{−1} in the potential window of 0.1–0.2 V relative to RHE. Additionally, electrochemical impedance spectroscopy (EIS) was collected from the frequency range of 0.01 Hz to 100 kHz, and the test voltage was −0.023 V (vs. RHE).

4. Conclusions

In this work, pH-universal Ru/C electrocatalysts for HER were constructed using a two-step adsorption–pyrolysis strategy. In 1.0 M KOH and 0.5 M H₂SO₄, the overpotentials of Ru_{0.3}/C–800 were as low as 29 mV and 83 mV to obtain a current density of 10 mA cm^{−2}. This work has several advantages over previously reported results: (1) The “starch strips” containing natural alkali metal additives (NaCl) were used as the raw material, which were green, ecofriendly, and economical. (2) The alkali metal auxiliaries were able to stabilize Ru and regulate the distribution of Ru valence, which contributed to the formation of more active components Ru⁰. (3) NaCl as a salt template could induce a porous structure, promoting mass transfer and exposing more active sites. The synthetic strategy was not only general and scalable but also emphasized the critical role of alkali metal in promoting HER activity, which provides a new idea for developing efficient non-Pt HER catalyts.

Supplementary Materials: The following supporting information can be downloaded at: <https://www.mdpi.com/article/10.3390/catal13030552/s1>, Table S1: Elemental content of Ru and Na measured by ICP-OES, Table S2: Ru⁰/Ru⁺ ratio of Ru_{0.3}/C–800, Ru_{0.3}/C–900, Ru_{0.3}/C–1000, and Ru_{0.3}/C–800–WF; Table S3: BET surface area (m²/g) of Ru_{0.3}/C–700, Ru_{0.3}/C–800, Ru_{0.3}/C–900, Ru_{0.3}/C–1000, and Ru_{0.3}/C–800–WF; Table S4: R_s and R_{ct} of Ru_{0.3}/C–800, Ru_{0.3}/C–900, and Ru_{0.3}/C–1000 in 1.0 M KOH; Table S5: Summary of the recently reported HER catalyts; Figure S1: TEM image of Ru_{0.3}/C–800, where the yellow circle is a pore structure, mainly mesopores; Figure S2: (a) TEM image of Ru_{0.2}/C–800, (b) TEM image of Ru_{0.4}/C–800; Figure S3: (a) TEM image of Ru_{0.3}/C–700, (b) TEM image of Ru_{0.3}/C–900, (c) TEM image of Ru_{0.3}/C–1000; Figure S4: TEM image of (a) Ru_{0.3}/C–800 and (b) Ru_{0.3}/C–800–WF; Figure S5: HRTEM of Ru_{0.3}/C–800; Figure S6: HRTEM image of (a) Ru_{0.3}/C–800 and (b) Ru_{0.3}/C–900; Figure S7: (a) XRD patterns of C–800, Ru_{0.2}/C–800, Ru_{0.3}/C–800, and Ru_{0.4}/C–800 (inset: XRD enlargement of Ru_{0.3}/C–800), (b) XRD patterns of Ru_{0.3}/C–800 and Ru_{0.3}/C–800–WF; Figure S8: (a) High-resolution XPS spectra of Na 1s of Ru_{0.3}/C–800, Ru_{0.3}/C–900, and Ru_{0.3}/C–1000, (b) high-resolution XPS spectra of Ru 3p of Ru_{0.3}/C–800, Ru_{0.3}/C–900, and Ru_{0.3}/C–1000; Figure S9: Raman spectra of Ru_{0.3}/C–700, Ru_{0.3}/C–800, Ru_{0.3}/C–900, and Ru_{0.3}/C–1000; Figure S10: LSV curves of Ru powder, Pt electrode, and Ru_{0.3}/C–800 in 1.0 M KOH; Figure S11: CV curves of (a) C–800, (b) Ru_{0.2}/C–800, (c) Ru_{0.3}/C–800, and (d) Ru_{0.4}/C–800 at different scan rates: 10, 20, 30, 40, and 50 mV s^{−1} in 1.0 M KOH solution; Figure S12: CV curves of (a) Ru_{0.3}/C–700, (b) Ru_{0.3}/C–900, and (c) Ru_{0.3}/C–1000 at different scan rates: 10, 20, 30, 40, and 50 mV s^{−1} in 1.0 M KOH solution, (d) linear plot of the capacitive current versus the scan rate for determination of the C_{dl}; Figure S13: EIS spectra of Ru_{0.3}/C–800, Ru_{0.3}/C–900, and Ru_{0.3}/C–1000 (inset: equivalent circuit models used for fitting the EIS response of HER); Figure S14: (a) Tafel plots of Ru_{0.3}/C–800 and Ru_{0.3}/C–800–WF, (b) CV curves of Ru_{0.3}/C–800–WF at different scan rates: 10, 20, 30, 40, and 50 mV s^{−1} in 1.0 M KOH solution, (c) linear plot of the capacitive current versus the scan rate for determination of the C_{dl}, (d) Nyquist plots of Ru_{0.3}/C–800 and Ru_{0.3}/C–800–WF; Figure S15: (a) LSV curves of Ru_{0.3}/C–800, Ru powder, Pt electrode, and 20 wt% Pt/C in 0.5 M H₂SO₄, (b) The i–t curve of Ru_{0.3}/C–800 in 0.5 M H₂SO₄; Figure S16: (a) LSV curves of Ru_{0.3}/C–800, Ru powder, Pt electrode, and 20 wt% Pt/C in 1.0 M PBS, (b) The i–t curve of Ru_{0.3}/C–800 in 1.0 M PBS.

Author Contributions: B.G., Writing—original draft, Investigation, and Visualization; C.Z., Investigation; Y.Z.: Investigation; J.G., Project administration; Z.W., Conceptualization, Writing—review, and Funding acquisition; J.W., Writing—review and editing, Investigation, Methodology, and Funding acquisition. All authors have read and agreed to the published version of the manuscript.

Funding: This work was supported by the National Natural Science Foundation of China (52002102 and 22008213), the Zhejiang Provincial Natural Science Foundation (LQ21B060005 and LQ19B030009), and the Fundamental Research Funds for the Provincial Universities of Zhejiang (RF-A2022011).

Data Availability Statement: Data will be made available upon request.

Conflicts of Interest: The authors declare that they have no known competing financial interests or personal relationships that could have appeared to influence the work reported in this paper.

References

1. Jiang, B.; Wang, Z.; Cheng, L.; Chen, Z.; Dong, Y.; Wang, X.; Wang, T.; Mao, X.; Gao, Y.; Xu, Z.; et al. Regulating charge distribution of Ru atoms in ruthenium phosphide/carbon nitride/carbon for promoting hydrogen evolution reaction. *J. Alloy. Compd.* **2023**, *939*, 168717. [[CrossRef](#)]
2. Abdollahi, A.; Ghaffarinejad, A.; Arabi, M. Electrodeposition of Ni-Fe on graphite rod as an efficient and binder-free electrocatalyst for oxygen and hydrogen evolution reactions. *J. Alloy. Compd.* **2023**, *937*, 168400. [[CrossRef](#)]
3. Wu, X.; Wang, Z.; Zhang, D.; Qin, Y.; Wang, M.; Han, Y.; Zhan, T.; Yang, B.; Li, S.; Lai, J.; et al. Solvent-free microwave synthesis of ultra-small Ru-Mo₂C@CNT with strong metal-support interaction for industrial hydrogen evolution. *Nat. Commun.* **2021**, *12*, 4018. [[CrossRef](#)] [[PubMed](#)]
4. Jiang, K.; Luo, M.; Liu, Z.; Peng, M.; Chen, D.; Lu, Y.-R.; Chan, T.-S.; de Groot, F.M.F.; Tan, Y. Rational strain engineering of single-atom ruthenium on nanoporous MoS₂ for highly efficient hydrogen evolution. *Nat. Commun.* **2021**, *12*, 1687. [[CrossRef](#)] [[PubMed](#)]
5. Liu, Y.; Li, W.; Wu, H.; Lu, S. Carbon Dots Enhance Ruthenium Nanoparticles for Efficient Hydrogen Production in Alkaline. *Acta Phys. Chim. Sin.* **2021**, *37*, 2009082. [[CrossRef](#)]
6. Zhou, S.; Jang, H.; Qin, Q.; Li, Z.; Kim, M.G.; Li, C.; Liu, X.; Cho, J. Three-dimensional hierarchical Co(OH)F nanosheet arrays decorated by single-atom Ru for boosting oxygen evolution reaction. *Sci. China Mater.* **2021**, *64*, 1408–1417. [[CrossRef](#)]
7. Zhang, J.; Mao, X.; Wang, S.; Liang, L.; Cao, M.; Wang, L.; Li, G.; Xu, Y.; Huang, X. Superlattice in a Ru Superstructure for Enhancing Hydrogen Evolution. *Angew. Chem. Int. Ed.* **2022**, *61*, e202116867. [[CrossRef](#)]
8. Feng, T.; Yu, G.; Tao, S.; Zhu, S.; Ku, R.; Zhang, R.; Zeng, Q.; Yang, M.; Chen, Y.; Chen, W.; et al. A highly efficient overall water splitting ruthenium-cobalt alloy electrocatalyst across a wide pH range *via* electronic coupling with carbon dots. *J. Mater. Chem. A* **2020**, *8*, 9638–9645. [[CrossRef](#)]
9. Anantharaj, S.; Noda, S. Appropriate Use of Electrochemical Impedance Spectroscopy in Water Splitting Electrocatalysis. *ChemElectroChem* **2020**, *7*, 2297–2308. [[CrossRef](#)]
10. Zhou, Y.; Xie, Z.; Jiang, J.; Wang, J.; Song, X.; He, Q.; Ding, W.; Wei, Z. Lattice-confined Ru clusters with high CO tolerance and activity for the hydrogen oxidation reaction. *Nat. Catal.* **2020**, *3*, 454–462. [[CrossRef](#)]
11. Tiwari, J.N.; Dang, N.K.; Sultan, S.; Thangavel, P.; Jeong, H.Y.; Kim, K.S. Multi-heteroatom-doped carbon from waste-yeast biomass for sustained water splitting. *Nat. Sustain.* **2020**, *3*, 556–563. [[CrossRef](#)]
12. Cai, C.; Liu, K.; Zhu, Y.; Li, P.; Wang, Q.; Liu, B.; Chen, S.; Li, H.; Zhu, L.; Li, H.; et al. Optimizing Hydrogen Binding on Ru Sites with RuCo Alloy Nanosheets for Efficient Alkaline Hydrogen Evolution. *Angew. Chem. Int. Ed.* **2022**, *61*, e202113664. [[CrossRef](#)]
13. Ren, R.; Wang, X.; Chen, H.; Miller, H.A.; Salam, I.; Varcoe, J.R.; Wu, L.; Chen, Y.; Liao, H.; Liu, E.; et al. Reshaping the Cathodic Catalyst Layer for Anion Exchange Membrane Fuel Cells: From Heterogeneous Catalysis to Homogeneous Catalysis. *Angew. Chem. Int. Ed.* **2021**, *60*, 4049–4054. [[CrossRef](#)]
14. Ha, Y.; Fei, B.; Yan, X.; Xu, H.; Chen, Z.; Shi, L.; Fu, M.; Xu, W.; Wu, R. Atomically Dispersed Co-Pyridinic N-C for Superior Oxygen Reduction Reaction. *Adv. Energy Mater.* **2020**, *10*, 2002592. [[CrossRef](#)]
15. Rapson, T.D.; Ju, H.; Marshall, P.; Devilla, R.; Jackson, C.J.; Giddey, S.; Sutherland, T.D. Engineering a solid-state metalloprotein hydrogen evolution catalyst. *Sci. Rep.* **2020**, *10*, 3774. [[CrossRef](#)]
16. Tong, Y.; Sun, Q.; Chen, P.; Chen, L.; Fei, Z.; Dyson, P.J. Nitrogen-Incorporated Cobalt Sulfide/Graphene Hybrid Catalysts for Overall Water Splitting. *ChemSusChem* **2020**, *13*, 5112–5118. [[CrossRef](#)]
17. Ding, R.; Lin, L.; Pei, C.; Yu, X.; Sun, Q.; Park, H.S. Hierarchical Architectures Based on Ru Nanoparticles/Oxygen-Rich-Carbon Nanotubes for Efficient Hydrogen Evolution. *Chem.—A Eur. J.* **2021**, *27*, 11150–11157. [[CrossRef](#)]
18. Jiao, J.; Zhang, N.; Zhang, C.; Sun, N.; Pan, Y.; Chen, C.; Li, J.; Tan, M.; Cui, R.; Shi, Z.; et al. Doping Ruthenium into Metal Matrix for Promoted pH-Universal Hydrogen Evolution. *Adv. Sci.* **2022**, *9*, 2200010. [[CrossRef](#)]
19. Su, P.; Pei, W.; Wang, X.; Ma, Y.; Jiang, Q.; Liang, J.; Zhou, S.; Zhao, J.; Liu, J.; Lu, G.Q. Exceptional Electrochemical HER Performance with Enhanced Electron Transfer between Ru Nanoparticles and Single Atoms Dispersed on a Carbon Substrate. *Angew. Chem. Int. Ed.* **2021**, *60*, 16044–16050. [[CrossRef](#)]
20. Wang, C.; Qi, L. Heterostructured Inter-Doped Ruthenium–Cobalt Oxide Hollow Nanosheet Arrays for Highly Efficient Overall Water Splitting. *Angew. Chem. Int. Ed.* **2020**, *59*, 17219–17224. [[CrossRef](#)]
21. Rao, Y.; Xu, L.; Zhou, M.; Yin, B.; Osuka, A.; Song, J. Expanded Azaporphyrins Consisting of Multiple BODIPY Units: Global Aromaticity and High Affinities Towards Alkali Metal Ions. *Angew. Chem. Int. Ed.* **2022**, *61*, e202206899. [[CrossRef](#)] [[PubMed](#)]
22. Nielsen, A. Review of ammonia catalysis. *Catal. Rev.* **1971**, *4*, 1–26. [[CrossRef](#)]
23. Williams, F.J.; Palermo, A.; Tracey, S.; Tikhov, M.S.; Lambert, R.M. Electrochemical Promotion by Potassium of the Selective Hydrogenation of Acetylene on Platinum: Reaction Studies and XP Spectroscopy. *J. Phys. Chem. B* **2002**, *106*, 5668–5672. [[CrossRef](#)]
24. García-Bordejé, E.; Dongil, A.B.; Conesa, J.M.; Guerrero-Ruiz, A.; Rodríguez-Ramos, I. Promotion of Ru or Ni on Alumina Catalysts with a Basic Metal for CO₂ Hydrogenation: Effect of the Type of Metal (Na, K, Ba). *Nanomaterials* **2022**, *12*, 1052. [[CrossRef](#)] [[PubMed](#)]
25. Su, L.; Liu, L.; Zhuang, J.; Wang, H.; Li, Y.; Shen, W.; Xu, Y.; Bao, X. Creating Mesopores in ZSM-5 Zeolite by Alkali Treatment: A New Way to Enhance the Catalytic Performance of Methane Dehydroaromatization on Mo/HZSM-5 Catalysts. *Catal. Lett.* **2003**, *91*, 155–167. [[CrossRef](#)]

26. Zhao, B.; Zhai, P.; Wang, P.; Li, J.; Li, T.; Peng, M.; Zhao, M.; Hu, G.; Yang, Y.; Li, Y.-W.; et al. Direct Transformation of Syngas to Aromatics over Na-Zn-Fe₅C₂ and Hierarchical HZSM-5 Tandem Catalysts. *Chem* **2017**, *3*, 323–333. [[CrossRef](#)]
27. Chen, I.; Chen, F.L. Effect of alkali and alkaline-earth metals on the resistivity to coke formation and sintering of nickel-alumina catalysts. *Ind. Eng. Chem. Res.* **1990**, *29*, 534–539. [[CrossRef](#)]
28. Gentner, T.X.; Mulvey, R.E. Alkali-Metal Mediation: Diversity of Applications in Main-Group Organometallic Chemistry. *Angew. Chem. Int. Ed.* **2021**, *60*, 9247–9262. [[CrossRef](#)]
29. Qin, R.; Zhou, L.; Liu, P.; Gong, Y.; Liu, K.; Xu, C.; Zhao, Y.; Gu, L.; Fu, G.; Zheng, N. Alkali ions secure hydrides for catalytic hydrogenation. *Nat. Catal.* **2020**, *3*, 703–709. [[CrossRef](#)]
30. Zhang, W.; Sun, M.; Yin, J.; Abou-Hamad, E.; Schwingenschlögl, U.; Costa, P.M.F.J.; Alshareef, H.N. A Cyclized Polyacrylonitrile Anode for Alkali Metal Ion Batteries. *Angew. Chem. Int. Ed.* **2021**, *60*, 1355–1363. [[CrossRef](#)]
31. Zimmermann, P.; Ar, D.; Rößler, M.; Holze, P.; Cula, B.; Herwig, C.; Limberg, C. Selective Transformation of Nickel-Bound Formate to CO or C–C Coupling Products Triggered by Deprotonation and Steered by Alkali-Metal Ions. *Angew. Chem. Int. Ed.* **2021**, *60*, 2312–2321. [[CrossRef](#)]
32. Ding, Y.; Guo, X.; Qian, Y.; Gao, H.; Weber, D.H.; Zhang, L.; Goodenough, J.B.; Yu, G. In Situ Formation of Liquid Metals via Galvanic Replacement Reaction to Build Dendrite-Free Alkali-Metal-Ion Batteries. *Angew. Chem. Int. Ed.* **2020**, *59*, 12170–12177. [[CrossRef](#)]
33. Zhang, L.; Jang, H.; Liu, H.; Kim, M.G.; Yang, D.; Liu, S.; Liu, X.; Cho, J. Sodium-Decorated Amorphous/Crystalline RuO₂ with Rich Oxygen Vacancies: A Robust pH-Universal Oxygen Evolution Electrocatalyst. *Angew. Chem. Int. Ed.* **2021**, *60*, 18821–18829. [[CrossRef](#)]
34. Zhang, S.; Wu, Z.; Liu, X.; Shao, Z.; Xia, L.; Zhong, L.; Wang, H.; Sun, Y. Tuning the interaction between Na and Co₂C to promote selective CO₂ hydrogenation to ethanol. *Appl. Catal. B Environ.* **2021**, *293*, 120207. [[CrossRef](#)]
35. Chen, J.; Wang, H.; Gong, Y.; Wang, Y. Directly immobilizing a Ru–tannic acid linkage coordination complex on carbon cloth: An efficient and ultrastable catalyst for the hydrogen evolution reaction. *J. Mater. Chem. A* **2019**, *7*, 11038–11043. [[CrossRef](#)]
36. Sun, S.-W.; Wang, G.-F.; Zhou, Y.; Wang, F.-B.; Xia, X.-H. High-Performance Ru@C₄N Electrocatalyst for Hydrogen Evolution Reaction in Both Acidic and Alkaline Solutions. *ACS Appl. Mater. Interfaces* **2019**, *11*, 19176–19182. [[CrossRef](#)]
37. Xu, C.; Ming, M.; Wang, Q.; Yang, C.; Fan, G.; Wang, Y.; Gao, D.; Bi, J.; Zhang, Y. Facile synthesis of effective Ru nanoparticles on carbon by adsorption-low temperature pyrolysis strategy for hydrogen evolution. *J. Mater. Chem. A* **2018**, *6*, 14380–14386. [[CrossRef](#)]
38. Kweon, D.H.; Okyay, M.S.; Kim, S.-J.; Jeon, J.-P.; Noh, H.-J.; Park, N.; Mahmood, J.; Baek, J.-B. Ruthenium anchored on carbon nanotube electrocatalyst for hydrogen production with enhanced Faradaic efficiency. *Nat. Commun.* **2020**, *11*, 1278. [[CrossRef](#)]
39. Li, J.-S.; Huang, M.-J.; Kong, L.-X.; Chen, X.-N.; Zhou, Y.-W.; Li, J.-L.; Wang, M.-Y. Ruthenium Nanoparticles Anchored on Graphene Hollow Nanospheres Superior to Platinum for the Hydrogen Evolution Reaction in Alkaline Media. *Inorg. Chem.* **2020**, *59*, 930–936. [[CrossRef](#)]
40. Chithaiah, P.; Binwal, D.C.; Raos, C.N.R. Simple Synthesis of 2D Molybdenum Carbide Nanosheets and Their Application in the Hydrogen Evolution Reaction. *Eur. J. Inorg. Chem.* **2022**, *2022*, e202101086. [[CrossRef](#)]
41. Song, H.; Wu, M.; Tang, Z.; Tse, J.S.; Yang, B.; Lu, S. Single Atom Ruthenium-Doped CoP/CDs Nanosheets via Splicing of Carbon-Dots for Robust Hydrogen Production. *Angew. Chem. Int. Ed.* **2021**, *60*, 7234–7244. [[CrossRef](#)] [[PubMed](#)]
42. Kong, X.; Xu, K.; Zhang, C.; Dai, J.; Oliaee, S.N.; Li, L.; Zeng, X.; Wu, C.; Peng, Z. Free-Standing Two-Dimensional Ru Nanosheets with High Activity toward Water Splitting. *ACS Catal.* **2016**, *6*, 1487–1492. [[CrossRef](#)]
43. Zheng, Y.; Jiao, Y.; Zhu, Y.; Li, L.H.; Han, Y.; Chen, Y.; Jaroniec, M.; Qiao, S.-Z. High Electrocatalytic Hydrogen Evolution Activity of an Anomalous Ruthenium Catalyst. *J. Am. Chem. Soc.* **2016**, *138*, 16174–16181. [[CrossRef](#)] [[PubMed](#)]
44. Dong, S.; Li, Y.; Zhao, Z.; Li, R.; He, J.; Yin, J.; Yan, B.; Zhang, X. A Review of the Application of Heterostructure Catalysts in Hydrogen Evolution Reaction. *ChemistrySelect* **2022**, *7*, e202104041. [[CrossRef](#)]
45. Lu, E.; Zhang, Z.; Tao, J.; Hou, Y.; Zhang, J.; Yu, Z. Enhanced Metal-Semiconductor Interaction for Photocatalytic Hydrogen Evolution Reaction. *Chem.—A Eur. J.* **2022**, *28*, e202201590. [[CrossRef](#)]
46. Chen, Z.; Liu, X.; Shen, T.; Wu, C.; Zu, L.; Zhang, L. Porous NiFe alloys synthesized via freeze casting as bifunctional electrocatalysts for oxygen and hydrogen evolution reaction. *Int. J. Hydrogen Energy* **2021**, *46*, 37736–37745. [[CrossRef](#)]
47. Wang, T.; Tao, L.; Zhu, X.; Chen, C.; Chen, W.; Du, S.; Zhou, Y.; Zhou, B.; Wang, D.; Xie, C.; et al. Combined anodic and cathodic hydrogen production from aldehyde oxidation and hydrogen evolution reaction. *Nat. Catal.* **2022**, *5*, 66–73. [[CrossRef](#)]
48. Liu, L.; Qin, C.; Yu, M.; Wang, Q.; Wang, J.; Hou, B.; Jia, L.; Li, D. Morphology Evolution of Hcp Cobalt Nanoparticles Induced by Ru Promoter. *ChemCatChem* **2020**, *12*, 2083–2090. [[CrossRef](#)]
49. Niyitanga, T.; Jeong, H.K. Modification of thermally reduced graphite oxide and molybdenum disulfide by solution plasma for hydrogen evolution reaction. *Mater. Chem. Phys.* **2021**, *263*, 124345. [[CrossRef](#)]
50. Ortiz-Restrepo, J.E.; Loaiza, O.A.; Urresta, J.D.; Velasquez, J.D.; Pastor, E.; Chaur, M.N.; Lizcano-Valbuena, W.H. A comparative study of different carbon materials as metal-free catalysts for oxygen reduction and hydrogen evolution reactions in alkaline media. *Diam. Relat. Mater.* **2021**, *117*, 108464. [[CrossRef](#)]

51. Pham, N.N.; Kang, S.G.; Kim, H.-J.; Pak, C.; Han, B.; Lee, S.G. Catalytic activity of Ni₃Mo surfaces for hydrogen evolution reaction: A density functional theory approach. *Appl. Surf. Sci.* **2021**, *537*, 147894. [[CrossRef](#)]
52. Zhu, T.; Huang, J.; Huang, B.; Zhang, N.; Liu, S.; Yao, Q.; Haw, S.; Chang, Y.; Pao, C.; Chen, J.; et al. High-Index Faceted RuCo Nanoscrews for Water Electrosplitting. *Adv. Energy Mater.* **2020**, *10*, 2002860. [[CrossRef](#)]

Disclaimer/Publisher's Note: The statements, opinions and data contained in all publications are solely those of the individual author(s) and contributor(s) and not of MDPI and/or the editor(s). MDPI and/or the editor(s) disclaim responsibility for any injury to people or property resulting from any ideas, methods, instructions or products referred to in the content.